Int J Adv Manuf Technol (2018) 94:3713–3730
DOI 10.1007/s00170-017-0964-z

ORIGINAL ARTICLE

Dissimilar friction-stir lap-welding of aluminum-magnesium (AA5052) and aluminum-copper (AA2024) alloys: microstructural evolution and mechanical properties

R. Rafiei[1,2] · **M. Shamanian**[1] · **M. H. Fathi**[1,3] · **F. Khodabakhshi**[4]

Received: 26 March 2017 / Accepted: 14 August 2017 / Published online: 24 September 2017

Abstract In this study, feasibility of dissimilar friction-stir welding between an Al-Mg alloy (AA5052-O) and an Al-Cu alloy (AA2024-T4) in the lap joint design was assessed. After establishing a suitable working window in the moderate heat inputs in the term of rotational speed (w) and traverse velocity (v) to attain a defect-free sound dissimilar weld between these alloys, the microstructural characteristics and mechanical properties were evaluated. A hardness loss in the thermo-mechanical-affected zone and heat-affected zone at the AA2024 side was noticed due to over-ageing of precipitates. The most of processed dissimilar welds were failed along the stir zone. Depending on the welding defects, different fractographic aspects were observed. The processing parameters were optimized as $w = 1250$ rpm and $v = 160$ mm/min, which its weld failed from the weakest base metal (i.e., AA5052). A joint strength ratio of ~ 99% (strength of~ 200 MPa) and a completely ductile fracture behavior with large dimple-like features were noticed.

Keywords Friction-stir welding · Dissimilar lap-joining · Microstructure · Mechanical property · Al-Mg alloy · Al-Cu alloy

1 Introduction

Aluminum and its alloys have been broadly utilized for a variety of several applications from very simple components to large complex ones such as an aircraft body [1]. In this regard, aluminum-magnesium (Al-Mg) and aluminum-copper (Al-Cu) alloys have been widely employed in many emerging fields of the aerospace, automotive, and marine industries for constructions of frames, pipelines, and storage-tanks [2]. Among different alloys of these two series, AA5052 and AA2024 are the two distinguished aluminum alloys which are mostly used in aircraft, automobile, and ship-building owing to their unique physical and mechanical properties [3]. AA5052 alloy is well-known, attributing to its exceptional corrosion resistance as well as good workability and weldability [4]. It can generally apply for fabrication of the aircraft fuel and oil lines, fuel tankages, and etc. [5]. However, the AA2024 aluminum alloy is mostly used in different industries due to its high strength to weight ratio [6].

To construct a complex geometry such as an airplane, an automobile, or a ship, it is required to join different metals and alloys in lap- or butt-joint designs [1]. Variety in the actual service conditions of different aluminum alloys and their intrinsic different properties became important in selecting of a proper joining process [7]. Dissimilar joining of aluminum alloys with fusion welding technologies would be very challenging with respect to the similar ones, mainly due to variations in the chemical composition and mechanical properties which leads to the formation of low melting temperature eutectic phases resulting in weld solidification hot cracking as

✉ R. Rafiei
rahimrafiei@shirazu.ac.ir

✉ F. Khodabakhshi
farzadkhodabakhshi83@gmail.com

[1] Department of Materials Engineering, Isfahan University of Technology, Isfahan 84156-83111, Iran

[2] Department of Materials Science and Engineering, School of Engineering, Shiraz University, Zand Boulevard, Shiraz, Iran

[3] Biomaterials Research Group, Department of Materials Engineering, Isfahan University of Technology, Isfahan 84156-83111, Iran

[4] School of Metallurgical and Materials Engineering, College of Engineering, University of Tehran, P.O. Box: 11155-4563, Tehran, Iran

Table 1 Chemical compositions for the examined AA5052 and AA2024 alloys sheets (wt%)

Materials	Elements						
	Cu	Mg	Si	Fe	Cr	Mn	Al
AA5052	0.009	2.620	0.159	0.229	0.19	0.198	Base
AA2024	4.134	1.405	0.159	0.347	0.0043	0.588	Base

well as the cold cracking caused by the intermetallic phases formation [8]. Therefore, solid-state joining processes are more interesting for the aim of dissimilar welding between these alloys [9]. Friction-stir welding (FSW) as a green, modern, and environment friendly solid-state joining technique has been introduced by The Welding Institute (TWI) in 1991 [10], mainly to join relatively light group of materials and especially aluminum and its alloys related to the object of the present study. In the FSW process, a non-consumable rotating tool composed of a shoulder and a pin is plunged into the contact faces of the plates to be welded [11]. After heat generation by rotation of the FSW tool in contact with the surfaces of base metals (BMs) due to friction and plastic deformation, a narrow column of plasticized material is formed around the tool [12]. With movement of the rotating tool along the contact line and forging of solidified materials from the advancing side toward the retreating edge, dissimilar joining is accomplished at solid-state below the melting points of BMs [13]. The microstructural developments during the welding process can be thereby influenced by the material flow pattern and temperature distribution affected by the main processing parameters as the tool rotational speed, traverse velocity, tool geometry, pin profile, shoulder diameter, pin diameter, pin length, shoulder to pin diameter ratio, and tilting angle [10]. Since, FSW as a solid-state joining technology do not involve melting and therefore overcome a variety of metallurgical problems such as porosity, segregation, brittle intermetallic phase's formation, weld solidification cracking, and heat-affected zone (HAZ) liquation cracking, it is ideally suited for welding of different aluminum alloys [14].

In the literature, FSW was introduced as an excellent solid-state welding process for joining of different aluminum alloys. However, the most of previous researches were focused on the similar FSW of aluminum alloys and there are relatively fewer reports about the dissimilar joining [15]. The same as conventional FSW of similar alloys, the tool design and processing conditions were found to significantly influence the strength of dissimilar welds [16]. Also, it is required to analyze the more welding features in the dissimilar welds of aluminum alloys. Although, the formation of intermetallic compound (IMC) layers between dissimilar

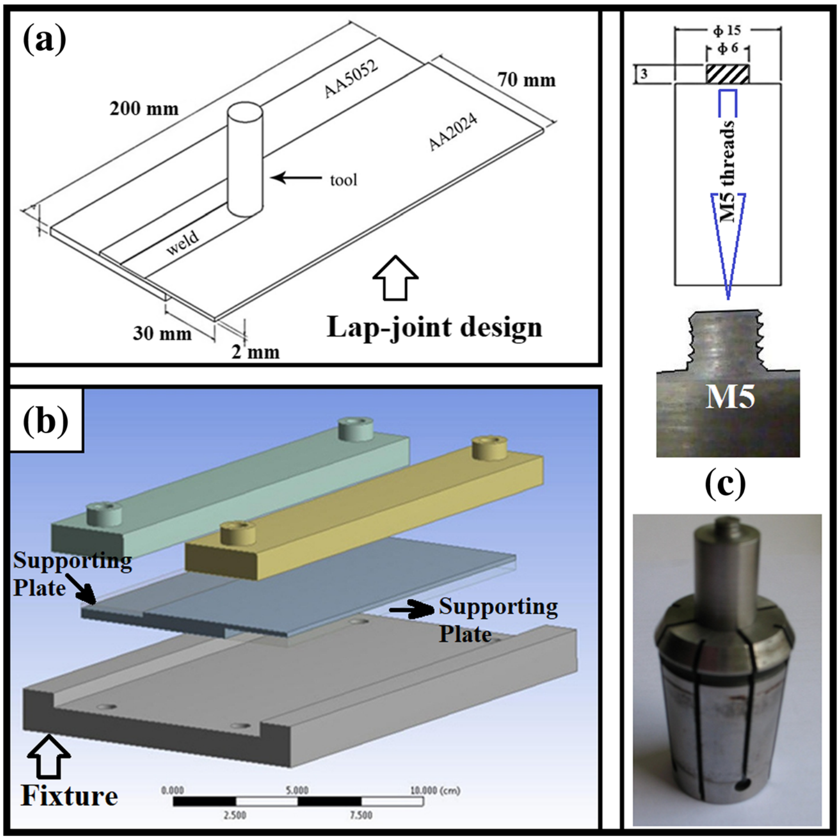

Fig. 1 **a** Schematic representation of the dissimilar lap joint design. **b** The employed fixture design for clamping of the sheets during the FSW process. **c** The image and geometry of the utilized FSW tool with identification of pin design and threads

Table 2 The main characteristics of the utilized AA5052 and AA2024 aluminum alloys: elastic modulus (*E*), yield strength (σ_y), ultimate tensile strength (σ_{UTS}), fracture stress (σ_f), elongation to fracture (*e*), and mean Vickers hardness (HV)

Material	Code	Condition	*E* (GPa)	σ_y (MPa)	σ_{UTS} (MPa)	σ_f (MPa)	*e* (%)	HV
Aluminum-magnesium alloy	AA5052	Annealed	70	70	201	160	41.3	51.5
Aluminum-copper alloy	AA2024	T4-temper	73	300	486	481	23.8	140.0

alloys as well as the solution/re-precipitation mechanisms have indicated very effective on the strength of dissimilar welds [17]. However, the influence of thermo-mechanical conditions depending on the welding processing parameters on these microstructural characteristics were not addressed well [16]. Generally, with increasing the frictional heat input, the thickness of IMC layers can be increased as well as the intensifying of over-ageing phenomena which can deteriorate the strength of dissimilar weld [18]. In the most of previous researches about FSW of dissimilar aluminum alloys which leads to the formation of dissimilar welds with exceptional joining efficiencies, significant mechanical mixing in the SZ due to a complex vortex, whorl, and swirl materials flow caused by the chaotic-dynamic mixing process exerted a remarkable effect on the resultant quality of the welded component [19].

Despite of some researches on the dissimilar friction-stir joining between the AA5xxx and AA2xxx alloys series [20, 21], to the best knowledge of the present authors, there is no report on the dissimilar friction-stir welding of AA5052 and AA2024 alloys. These alloys are rapidly employed beside each other in several automotive, rail transportation, and aerospace applications. Dissimilar welding of AA5052 and AA2024 alloys to attain a good combination of corrosion resistance and strength in one component is a very attractive research object. However, joining of these two alloys with conventional fusion welding processes is not possible. Furthermore, despite of the wide usage for industrial application of bi-metallic components from Al-Mg and Al-Cu alloys, there were not enough studies about dissimilar welding of these alloys [21]. We aimed to contribute from the knowledge of similar friction-stir welding for AA5052 and AA2024 alloys to fulfill the deficiency of knowledge for dissimilar FSW of these alloys. In this study, metallurgical characteristics of the dissimilar friction-stir lap-welded joints between AA5052 and AA2024 alloys sheets were examined to evaluate the performance and characteristics of these welded joints and results inferred. The effects of processing parameters on the microstructure and mechanical properties of dissimilar FSWed AA5052-AA2024 joints were studied, as well. Tool rotational speed (*w*) and traverse velocity (*v*) as the main processing parameters were optimized to obtain a sound defect-free dissimilar FSW between these alloys with tolerable mechanical performance. As a crucial issue, the effects of lapping sequence for the upper and lower sheets on the formation of welding defects during friction-stir lap-welding of dissimilar aluminum alloys and subsequent mechanical properties were examined [22]. Therefore, in this research, the influence of lapping sequence and welding speeds on the main lap-weld defect features of hook and voids and following tensile strength of

Fig. 2 Schematic view of the K-type thermocouples locations for measuring the temperature profiles at advancing side, retreating side, and center line positions during FSW process

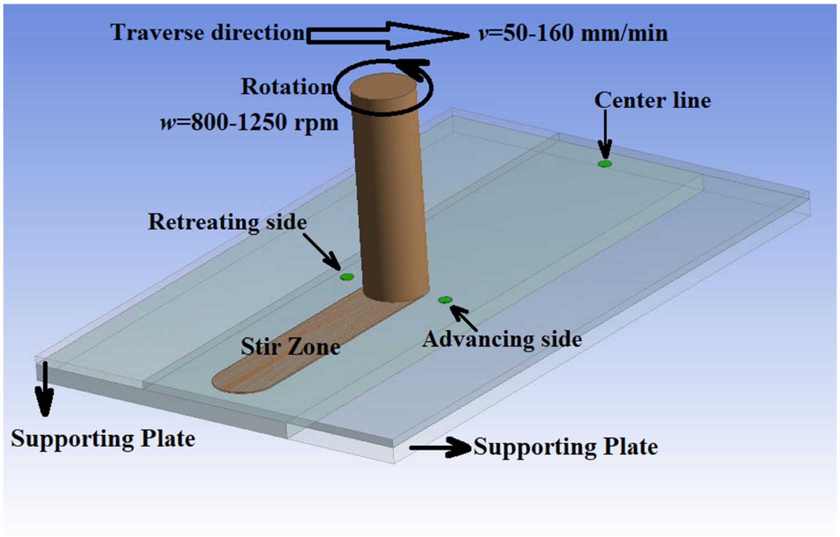

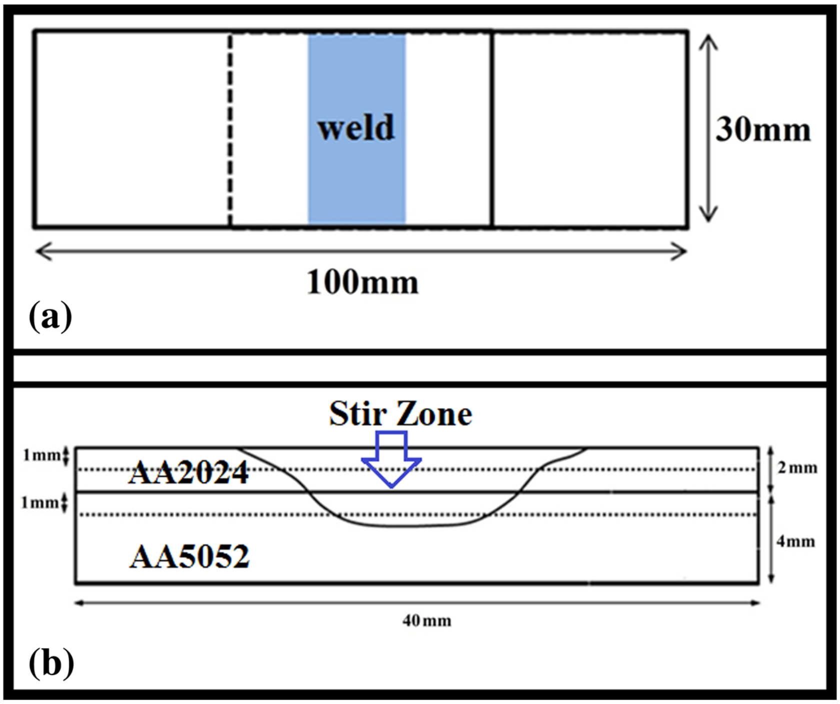

Fig. 3 Sample preparation for **a** transverse tensile testing and **b** indentation Vickers microhardness measurement

joints were discussed in detail, as well [23]. A comprehensive discussion was presented to address the influence of weld integrity and microstructure on the strength of these dissimilar FSWed joints at these optimum welding conditions with establishing a microstructure-mechanical properties relationship.

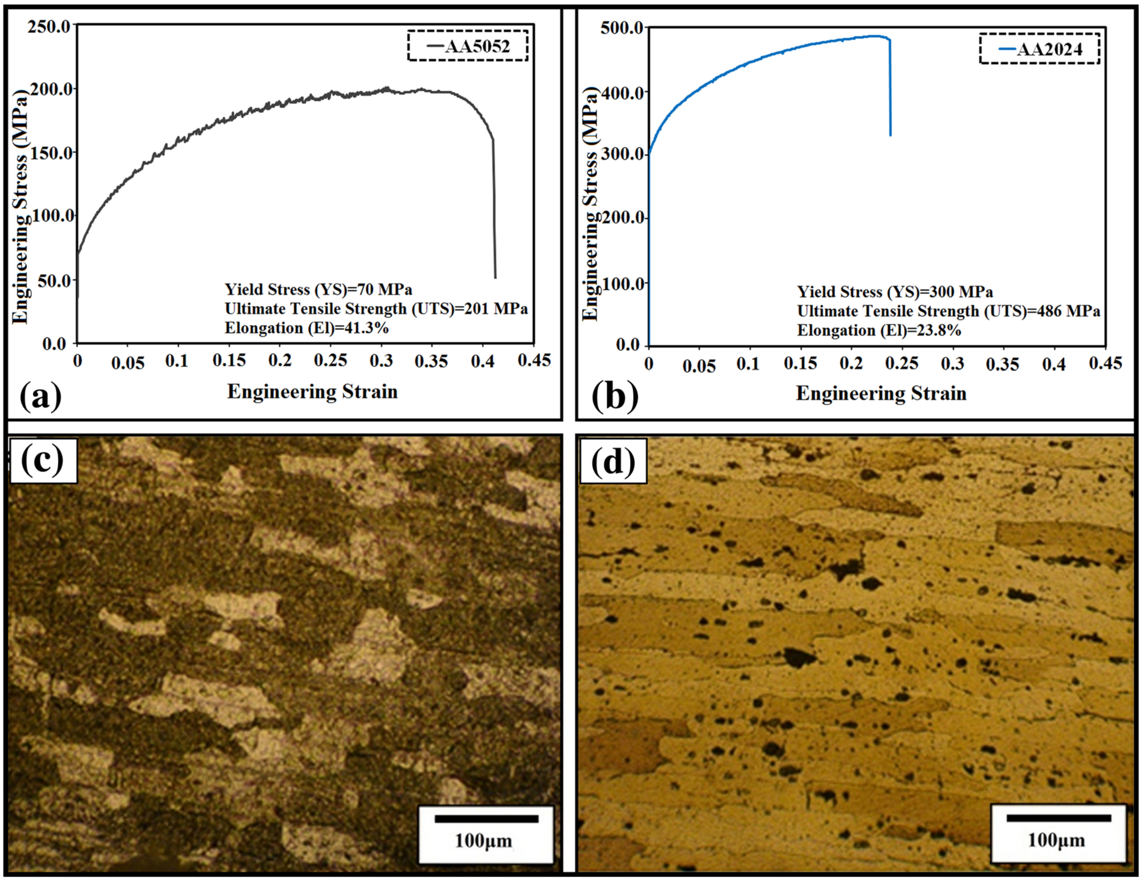

Fig. 4 **a**, **b** Engineering stress-strain curves and **c**, **d** optical microstructures of the initial AA5052-O and AA2024-T4 aluminum alloys, respectively

2 Materials and methods

The sheets of aluminum-magnesium alloy (AA5052) and aluminum-copper alloy (AA2024) in the annealed (O) and natural aged (T4) conditions were supplied with the thicknesses of 4 and 2 mm, respectively. Chemical compositions of these alloys are expressed in Table 1. These sheets were cut into the small samples with a cross-sectional area of 200 × 70 mm^2. A traditional vertical milling chuck machine was used for the aim of dissimilar friction-stir welding (FSW) between these Al-Mg and Al-Cu alloys. Both of the sheets of these alloys were grinded by 320 grit SiC papers and cleaned in acetone before application. A lap joint design with an overlapping area of 200 × 40 mm^2 was used for the aim of dissimilar welding, as schematically shown in Fig. 1a. As reported in Table 2 and discussed in the text, the hardness and tensile strength of AA2024-T4 are more than three times higher than the AA5052-O alloy. Consequently, by locating the annealed Al-Mg alloy on the top side in the lap joint design, the generated heating cycle is not adequate to soften and plasticize the tempered Al-Cu alloy [10]. Therefore, joining was not possible in that condition. After several examinations, it was found that for occurrence of bonding between these dissimilar metals, the AA2024 alloy must be located on the top of the AA5052 alloy in contact with the shoulder of the FSW tool, as shown in Fig. 1a. It can be due to the extremely higher strength of the AA2024-T4 alloy rather than the AA5052-O alloy. An especially designed fixture was used for clamping of the sheets with dissimilar lap joint design during the FSW process, as schematically drawn in Fig. 1b. The FSW tool was made from hot-working high strength H13 steel with a hardness of around 45 HRC. The main specifications of this FSW tool includes the shoulder diameter of 15 mm, pin diameter of 6 mm, and pin height of 3 mm with M5 threads, as the geometrical dimensions and macro-images of the tool and threads are presented in Fig. 1c. The presence of threads on the FSW tool can accelerate the materials upward, downward, and inter-mixing flows by applying the forging force and tool stirring action simultaneously. The existence of M5 threads on the pin of cylindrical tools to promote

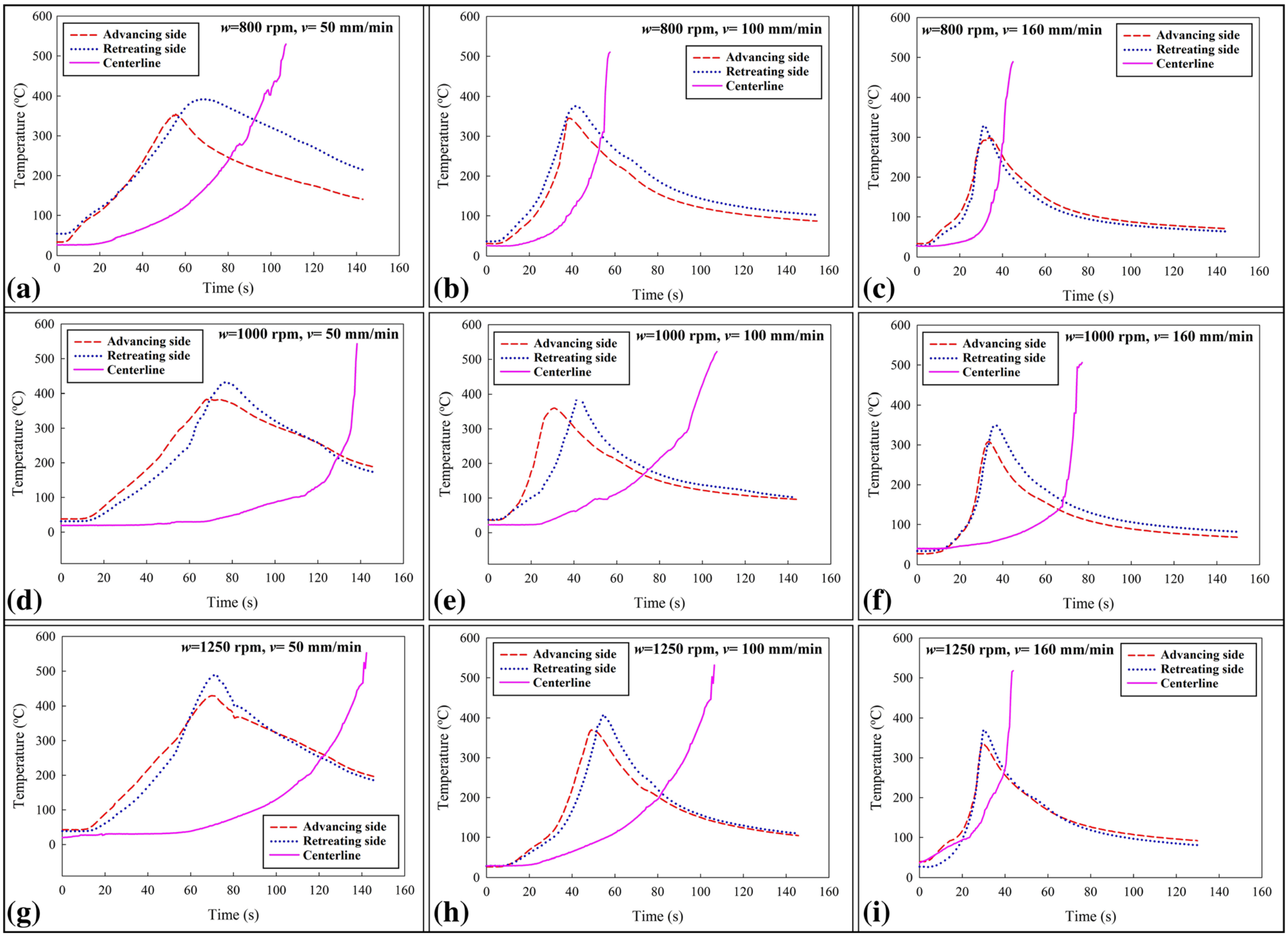

Fig. 5 Temperature-time profiles for advancing side, retreating side, and centerline of the dissimilar FSWed joints at various ranges of rotational speed and traverse velocity: **a** w=800 rpm/v=50 mm/min, **b** w=800 rpm/v=100 mm/min, **c** w=800 rpm/v=160 mm/min, **d** w=1000 rpm/v=50 mm/min, **e** w=1000 rpm/v=100 mm/min, **f** w=1000 rpm/v=160 mm/min, **g** w=1250 rpm/v=50 mm/min, **h** w=1250 rpm/v=100 mm/min, and **i** w=1250 rpm/v=160 mm/min

the material mixing during the FSW process is a well-known technical design issue [24]. A tilting angle of about 3 ° was kept constant during the FSW process. The effects of the main FSW parameters, i.e., tool rotational speed (*w*) and traverse velocity (*v*), on the microstructural characteristics and mechanical properties of the dissimilar FSWed joints were assessed. Various ranges of *w* (800–1250 rpm) and *v* (50–160 mm/min) parameters were examined for obtaining a suitable working window to process the defect-free sound dissimilar FSWs with acceptable mechanical performance. Moreover, the thermal cycles during the FSW process from the advancing side, retreating side, and center line in the front of the FSW tool at different processing parameters were monitored by placing three K-type thermocouples at these regions as schematically shown in Fig. 2, and using from a computer aided data-acquisition system (Advantech USB 4718; Advantech America, Milpitas, CA), which was able to record 10 data per second.

After processing of dissimilar FSWs at various ranges of *w* and *v* parameters, microstructural characterization and mechanical testings were performed to elaborate the durability of processed dissimilar joints. For microstructural examinations, dissimilar joints were cross-sectioned perpendicular to the FSW direction, at first. Then, the standard metallographic procedure was employed on the prepared samples, i.e., mechanical grinding by using different grades of SiC papers and mechanical polishing by using diamond pastes down to the size of ~ 1 μm. Thereafter, these polished and cleaned samples were etched by using a modified Poulton's chemical reagent to reveal their macro- and microstructures. The microstructures of different regions across the dissimilar FSWed joints including base metal (BM), heat-affected zone (HAZ), thermo-mechanical-affected zone (TMAZ), and stir zone (SZ) were observed under a NIKON optical microscope (NIKON Model Epiphot 300, Japan). The average grain size of SZ under different processing parameters was determined by the mean linear intercept method according to the ASTM E3 Standard. To examine the evolutions in the structure of precipitates for AA5052 and AA2024 alloys before and after the FSW process, field emission-scanning electron microscopy (FE-SEM, Philips, Netherlands) analysis was accomplished. The material flow pattern and dissimilar metals intermixing were studied by using these OM and SEM characterizations, as well. To assess the mechanical performance of dissimilar FSWed joints, indentation hardness and transverse tensile testings were performed. Sample preparation for transverse tensile testing is shown in Fig. 3a. Tensile-shear loading on these prepared coupons was carried out with using a Hounsfield Universal Tensile Loading Machine (Hounsfield H50KS, USA) with a cross-head speed of 1 mm/min. The main findings from the occurrence of transverse tensile-shear testing on the prepared dissimilar joints were the failure location as well as the corresponding mechanical strength. After tensile rupture, the failure location was studied by using FE-SEM analysis, as well. The Vickers microhardness measurements were performed across the

Table 3 Influence of rotational speed and traverse velocity on the peak temperature at advancing side, retreating side, and center line of the dissimilar FSWed AA5052-AA2024 joints

Traverse velocity (*v*)	Rotational speed (*w*)								
	Advancing side			Retreating side			Center line		
	w = 800 rpm	*w* = 1000 rpm	*w* = 1250 rpm	*w* = 800 rpm	*w* = 1000 rpm	*w* = 1250 rpm	*w* = 800 rpm	*w* = 1000 rpm	*w* = 1250 rpm
v = 50 mm/min	355 °C	385 °C	430 °C	392 °C	434 °C	492 °C	523 °C	543 °C	550 °C
v = 100 mm/min	343 °C	362 °C	373 °C	377 °C	398 °C	404 °C	526 °C	536 °C	533 °C
v = 160 mm/min	299 °C	307 °C	336 °C	330 °C	349 °C	371 °C	488 °C	506 °C	518 °C

thickness section of processed dissimilar FSWed joints from AA2024 and AA5052 regions along two lines 1 mm below the top surface and joint interface, respectively. These measurement paths are plotted in Fig. 3b. A Buehler Micromet 5101 machine (Buehler, Germany) was used for doing these measurements. For estimating the indentation Vickers hardness of each point, load and dwell time were kept about 100 g and 10 s, respectively.

3 Results

3.1 Characteristics of the initial AA5052 and AA2024 aluminum alloys

Engineering stress-strain curves and optical microstructures of the examined AA5052-O and AA2024-T4 aluminum alloys are presented and compared in Fig. 4. Also, the main tensile properties and Vickers indentation resistance of these two alloys are reported in Table 2. A considerable difference between the mechanical properties of these BMs can be noticed. As seen, yield stress (YS) of the AA2024 alloy in T4 temper condition was more than four times higher than the AA5052 alloy in the annealed condition. Also, its ultimate tensile strength (UTS) and Vickers hardness were about 240 and 270% higher, respectively. Although, elongation of AA2024-T4 alloy was approximately half of the AA5052-O alloy. An equiaxed microstructure with the average grain size of ~ 50 μm was observed for the AA5052-O alloy. While, the grain structure of the AA2024-T4 alloy was elongated along the rolling direction and pinned by the copper aluminide (Al_2Cu) precipitates. As seen, these examined initial alloys exhibited the significant different mechanical properties. Therefore, solid-state friction-stir welding of these dissimilar alloys together would be very challenging and really interesting.

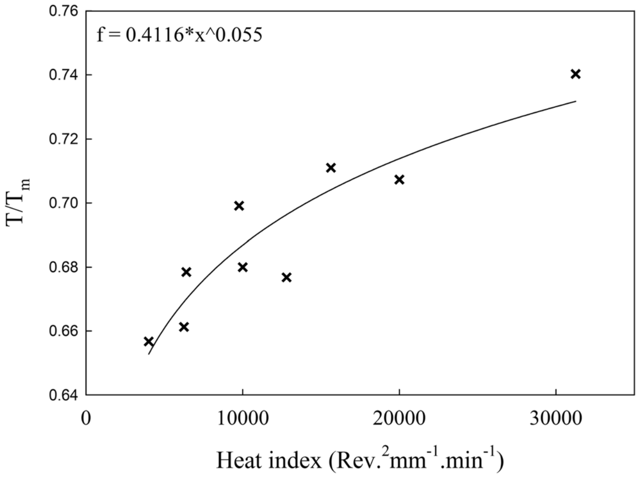

Fig. 6 Variations of the peak temperature at center line versus the processing heat input

3.2 Thermal cycles and dissimilar materials flow pattern

It is well established that the materials flow pattern and subsequent mechanical properties of the prepared dissimilar joints are controlled by the thermo-mechanical history during the FSW process [10]. Hence, we have monitored the thermal cycles during the dissimilar joining process at different regions of the welded samples. In Fig. 5, the influence of tool rotational speed and traverse velocity on the temperature profiles from the advancing side, retreating side, and center line of the dissimilar FSWed joints is demonstrated. Also, peak temperature as the main thermal data during the FSW process has been extracted from these curves and reported in Table 3 for different processing parameters. As can be found, for all regions with increasing the *w* and decreasing *v*, the peak temperature was improved, continuously. Furthermore, the effect of the *w*/*v* ratio as the heat index on the peak temperature with respect to the melting point of base alloys is plotted in Fig. 6, which shows a continuous increscent trend. The maximum

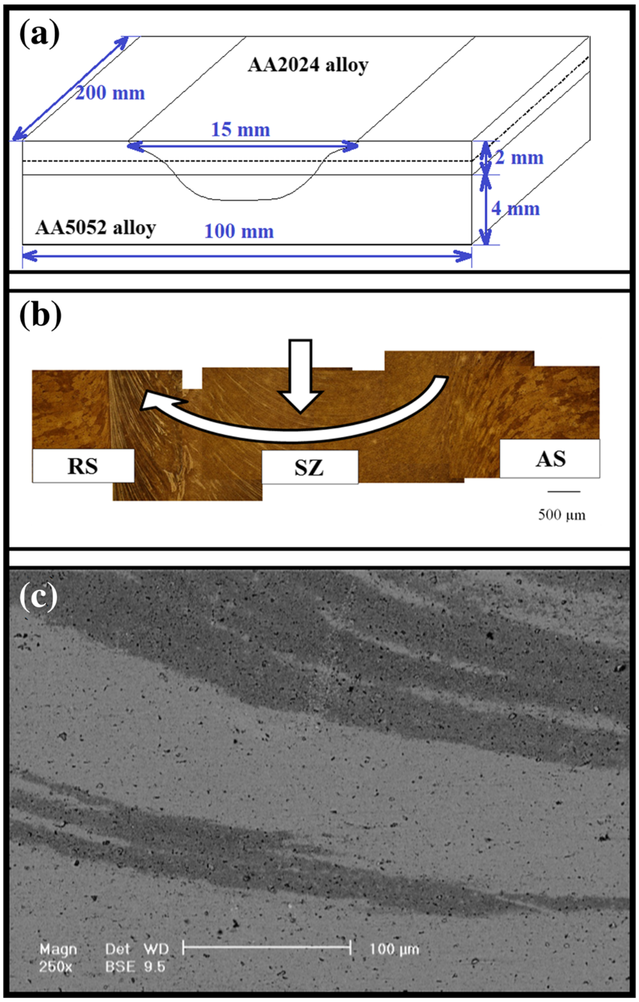

Fig. 7 **a** Schematic representation of the expected SZ flow patter between the dissimilar materials. **b** Optical macrograph and **c** SEM micrograph from the top surface a dissimilar FSW

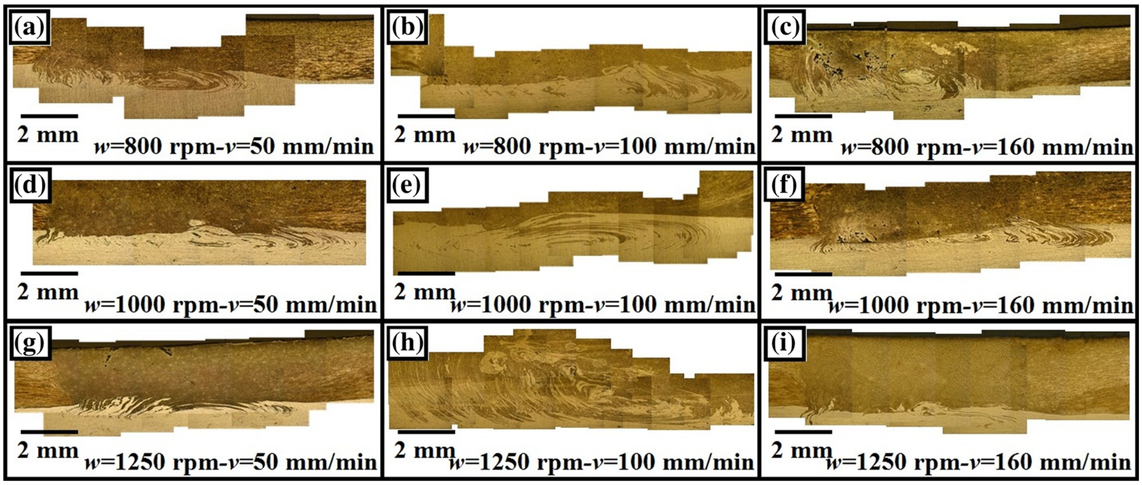

Fig. 8 Influence of tool rotational speed and traverse velocity on the SZ flow pattern across the thickness section of the dissimilar FSWed joints: **a** w=800 rpm/v=50 mm/min, **b** w=800 rpm/v=100 mm/min, **c** w=800 rpm/v=160 mm/min, **d** w=1000 rpm/v=50 mm/min, **e** w=1000 rpm/v=100 mm/min, **f** w=1000 rpm/v=160 mm/min, **g** w=1250 rpm/v=50 mm/min, **h** w=1250 rpm/v=100 mm/min, and **i** w=1250 rpm/v=160 mm/min

attained peak temperature was approximately around 550 °C which was achieved at the highest *w*/*v* ratio of 25 rpm.min/mm (i.e., *w* = 1250 rpm and *v* = 50 mm/min). Surface and thickness cross-sectional materials flow patterns for the dissimilar FSWed joints are presented in Figs. 7 and 8, respectively. In the flow patterns from the surface of processed dissimilar joints (Fig. 7), formation and elongation of grain structure from the advancing side toward the stir zone and retreating side were observed. Across the thickness section, it can be seen that the material flow patterns and inter-mixing were completely different at various ranges of rotational speed and traverse velocity, as shown in Fig. 8. Also, a close relationship between these material flow patterns across the thickness section and the reported temperature profiles can be found (see Figs. 6 and 8). Higher peak temperature during the process by higher *w* and lower *v* parameters leads to more materials softening and easier flow. A vortex materials flow was occurred at moderate heat inputs which exhibit two opposite effects on the dissimilar joining process. It means that it can increase the mechanical interlocking and thus enhance the bonding mechanism. While, in the other side by formation of cavities and tunneling defects, it can diminish the dissimilar joint soundness and mechanical performance. As can be found by comparing the thickness macro cross-sections of the dissimilar FSWed joints presented in Fig. 8, a completely sound and defect-free dissimilar weld between AA5052 and AA2024 alloys with an exceptional interfacial bonding was attained by employing the FSW parameters of *w* = 1250 rpm and *v* = 160 mm/min (i.e., *w*/*v* ratio of 7.8 rpm.min/mm). Formation of macro-mechanical interlocking at the interface of this dissimilar joint at higher magnification is shown in Fig. 9a. Furthermore, microstructures at advancing and retreating

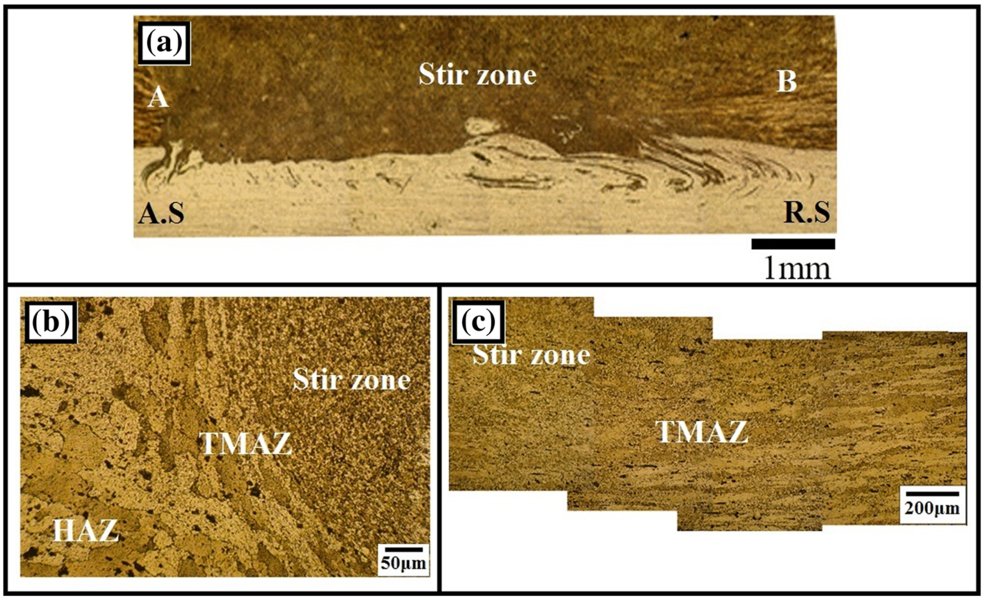

Fig. 9 **a** Optical macrograph showing the formation of macro-mechanical interlocks between AA5052 and AA2024 alloys at SZ for the dissimilar FSWed joint at processing conditions of *w* = 1250 rpm and *v* = 160 mm/min. Optical microstructures of HAZ and TMAZ regions at **b** advancing and **c** retreating sides, respectively

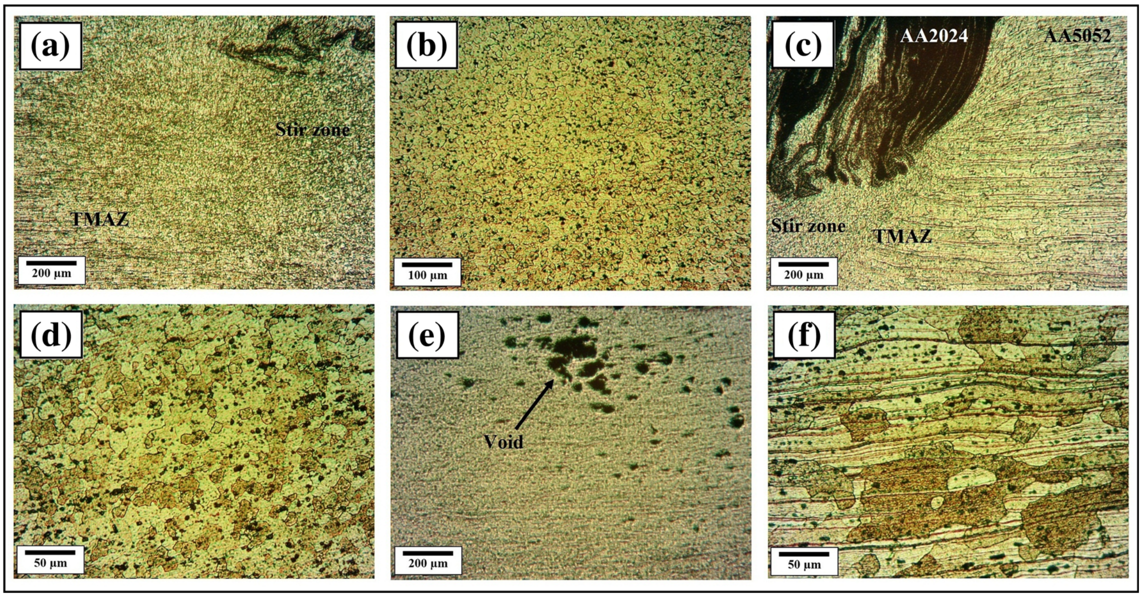

Fig. 10 Optical micrographs showing the microstructures of different regions across the dissimilar FSWed joint at $w = 800$ rpm and $v = 160$ mm/min. **a** TMAZ/SZ at advancing side, **b** SZ, **c** TMAZ/SZ at retreating side, **d** SZ at high magnification, **e** void and tunneling defect at SZ, and **f** HAZ

sides of this sample are presented in Fig. 9b, c, respectively. A sharp interface at the advancing side and an elongated grain structure at the retreating side can be observed, as well.

3.3 Microstructural developments

The effects of processing heat input in the terms of the w/v ratio on the microstructure of different BM, HAZ, TMAZ, and SZ regions across the dissimilar FSWed joints are demonstrated in Figs. 10, 11, and 12. Formation of some voids within the SZ of the processed sample at high traverse velocity and low heat input is shown in Fig. 10. For the other two processed samples at higher heat inputs, SZs seems mostly defect-free. In all the samples, it can be seen that from BM toward HAZ, TMAZ, and SZ the microstructure was continuously refined. As it is well know, the microstructural refinements during the FSW process can be attributed to the high temperature severe plastic deformation action of the rotating tool and occurrence of dynamic recrystallization (DRX) mechanisms [25]. Also, in the previous presented microstructural images, it can be found

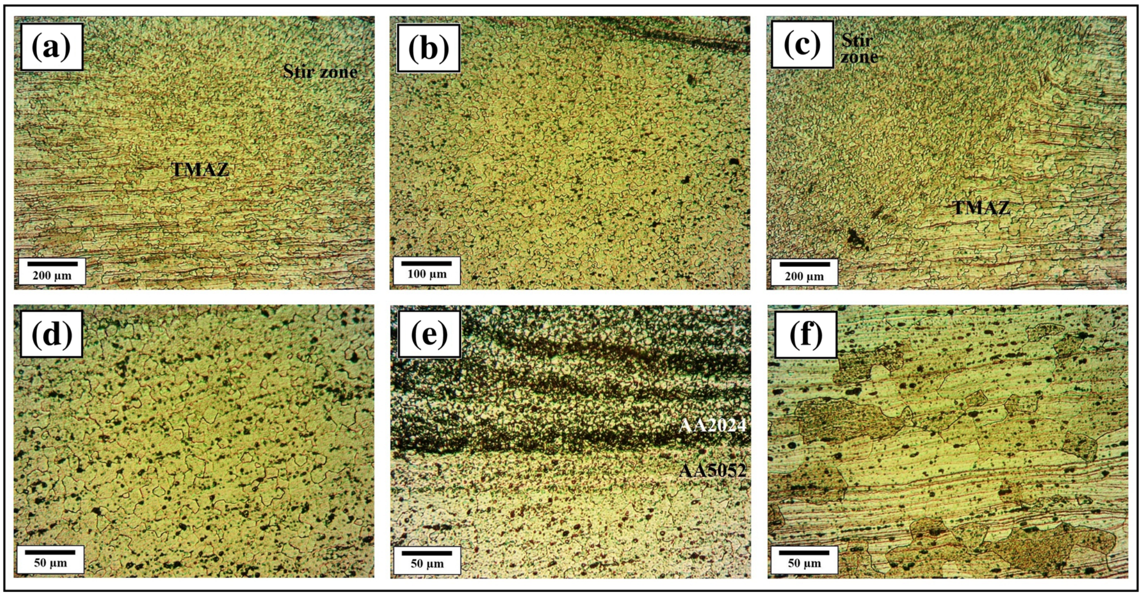

Fig. 11 Optical micrographs showing the microstructures of different regions across the dissimilar FSWed joint at $w = 800$ rpm and $v = 50$ mm/min. **a** TMAZ/SZ at advancing side; **b** SZ; **c** TMAZ/SZ at retreating side; **d**, **e** SZ at higher magnifications; and **f** HAZ

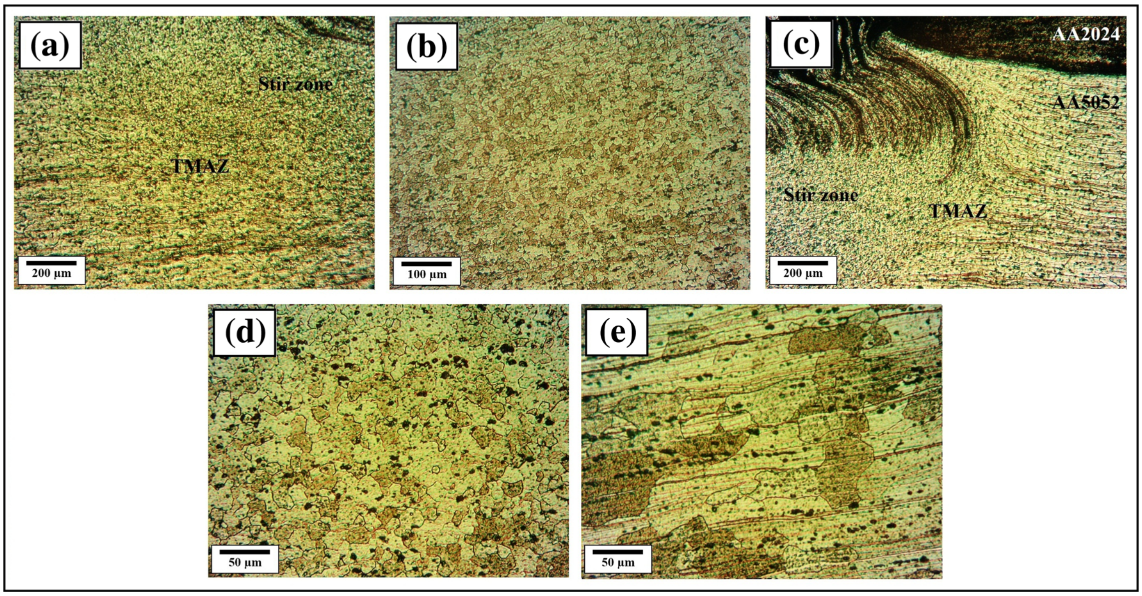

Fig. 12 Optical micrographs showing the microstructures of different regions across the dissimilar FSWed joint at $w = 1250$ rpm and $v = 50$ mm/min. **a** TMAZ/SZ at advancing side, **b** SZ, **c** TMAZ/SZ at retreating side, **d** SZ at high magnification, and **e** HAZ

that at the mechanical interlock regions, grain structural refinements have been intensified which can be due to the plastic constraint effect of the diffused interlocks [23]. Statistical distribution of aspect ratio for the grains within the SZ of dissimilar FSWed joint in the w/v ratio of 10 rpm.min/mm at the AA2024 side is plotted in Fig. 13. As shown, the most of grains possesses an aspect ratio of around 1, which means that the grain structure of SZ was mostly equiaxed. Effects of tool rotational speed and traverse velocity on the microstructure of SZ for these dissimilar FSWed joints are presented in Fig. 14a–d. For different processing conditions, the mean grain size was varied in the range of 3 to 5 µm. As seen, with decreasing w and increasing v, or increasing of heat input in terms of the w/v ratio, the microstructure of SZ was continuously refined.

3.4 Precipitate structures

FE-SEM images from the SZ flow pattern, interlock regions, and distribution of different precipitates within the metal matrix for the processed dissimilar joints at various ranges of FSW parameters are presented and compared in Figs. 15, 16, and 17. As can be seen, the formation and morphology of micro-mechanical interlocks at the interface of two alloys were affected by the processing parameters, significantly. With increasing w and also increasing v, interlocks became finer and the number of them was increased, which assisted to accelerate the bonding mechanisms between these dissimilar AA5052 and AA2024 alloys. According to these images, the best condition for dissimilar joining was occurred for the highest w and v values with moderate heat

Fig. 13 The distribution histogram of aspect ratio for grains within the SZ at the AA2024 side for the dissimilar FSWed joint at $w = 1000$ rpm and $v = 100$ mm/min

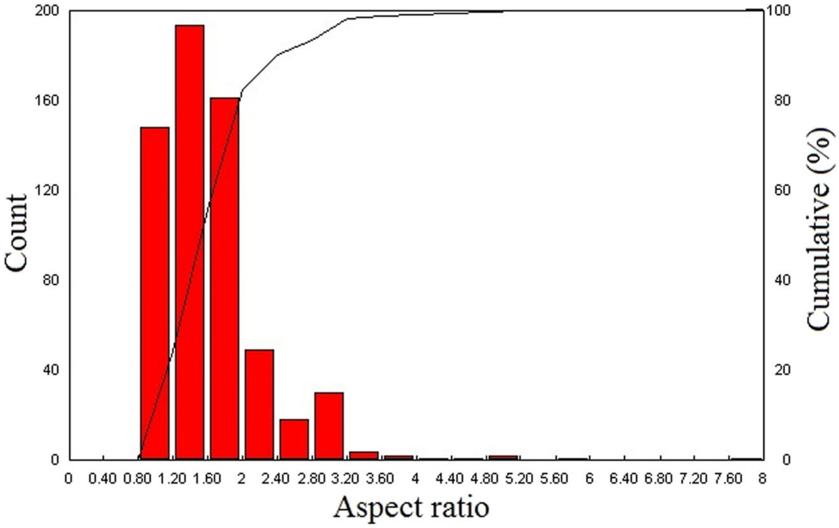

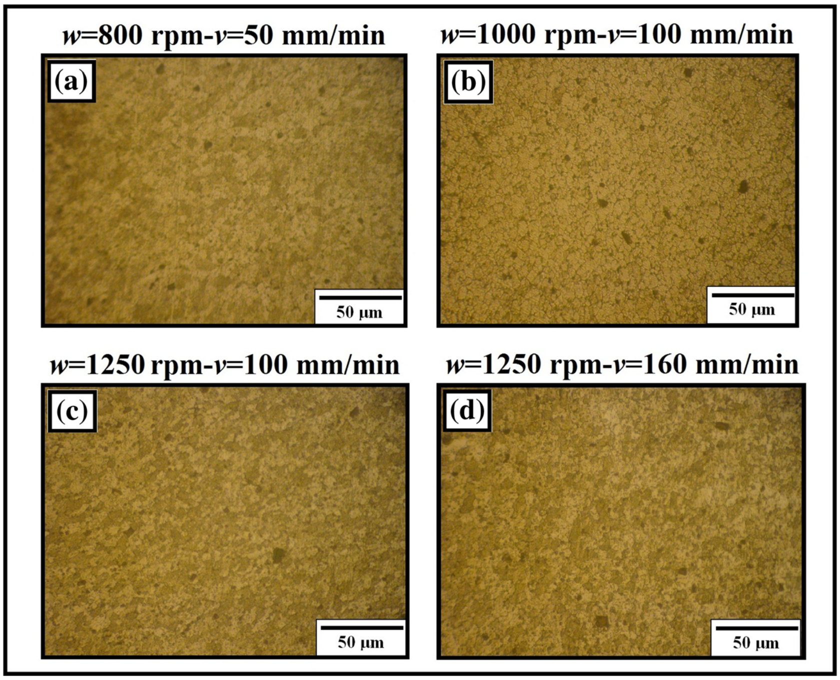

Fig. 14 Influence of tool rotational speed and traverse velocity on the grain structure of SZ for dissimilar FSWed joints: **a** w=800 rpm/v=50 mm/min, **b** w=1000 rpm/v=100 mm/min, **c** w=1250 rpm/v=100 mm/min, and **d** w=1250 rpm/v=160 mm/min

input values, i.e., w = 1250 rpm and v = 160 mm/min. Moreover, the precipitate structure and morphology after employing of the FSW process at different parameters were changed. These developments were mainly occurred at the precipitation-hardened AA2024 side of dissimilar joints. For the study of these modifications in the structure of precipitates with more detail, energy-dispersive X-ray spectroscopy (EDS) analysis was employed, as the elemental EDS mapping analysis results are presented in Fig. 18. As can be found, the most of large second-phase particles are some precipitates between Al-Fe and Al-Cu elements. They can probably be the Al_3Fe and Al_2Cu phases, respectively [26]. Moreover, some fine and spherical Si-rich precipitates are seen within the microstructure as well, which can be a phase between Mg and Si elements, such as the Mg_2Si precipitate.

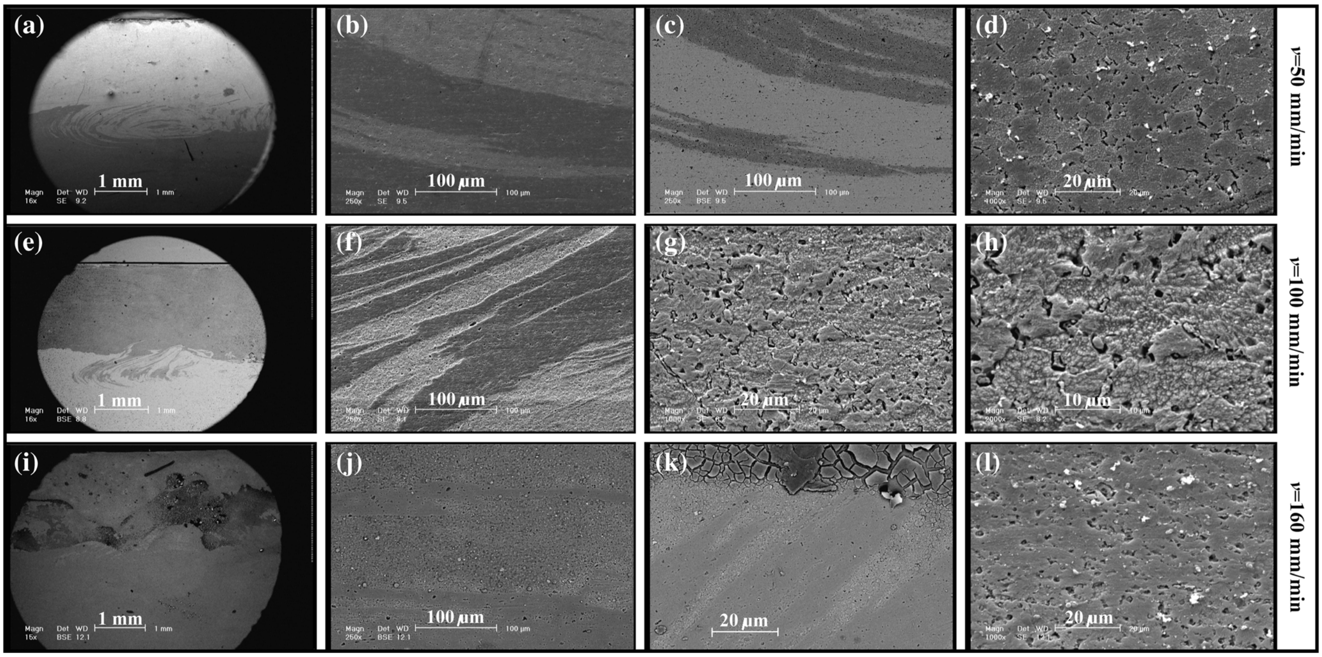

Fig. 15 Effects of traverse velocity on the SZ flow pattern, microstructure, and precipitates morphology for the dissimilar FSWed joints at rotational speed of 800 rpm. **a**–**d** v = 50 mm/min, **e**–**h** v = 100 mm/min, and **i**–**l** v = 160 mm/min

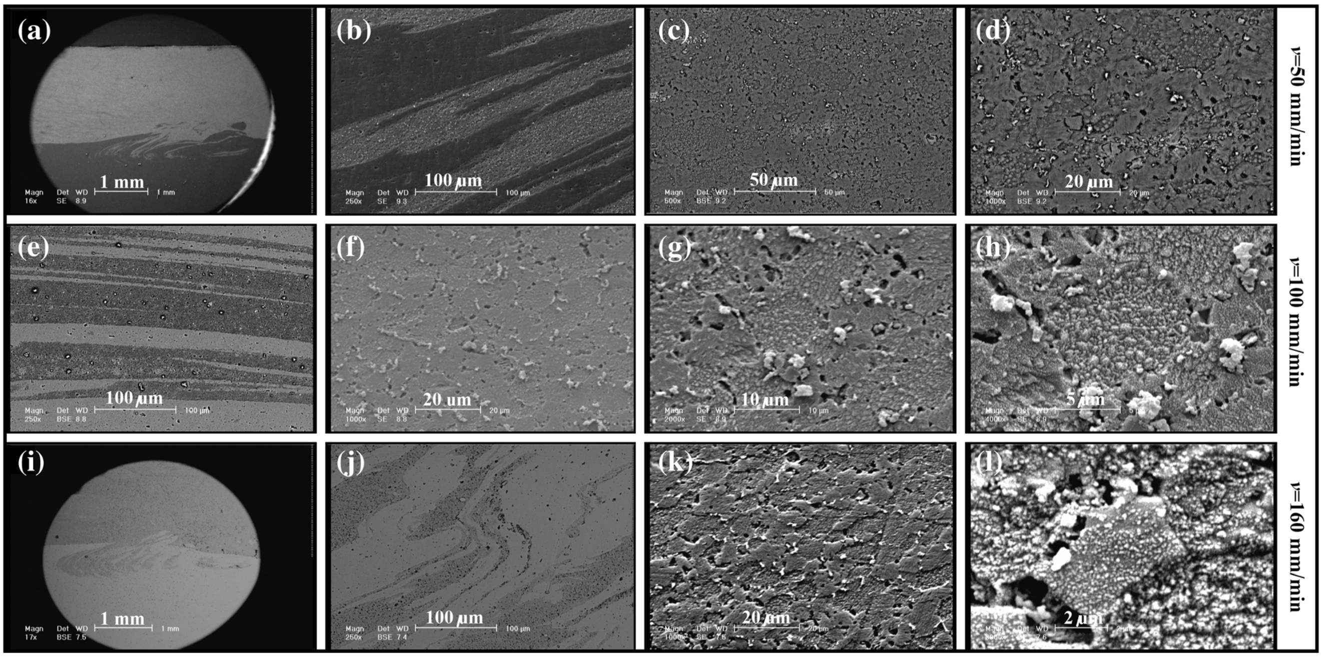

Fig. 16 Effects of traverse velocity on the SZ flow pattern, microstructure, and precipitates morphology for the dissimilar FSWed joints at rotational speed of 1000 rpm. **a**–**d** $v = 50$ mm/min, **e**–**h** $v = 100$ mm/min, and **i**–**l** $v = 160$ mm/min

3.5 Indentation resistance

Vickers indentation microhardness profiles for the dissimilar FSWed joints at different rotational speeds and traverse velocities from the AA2024 and AA5052 alloys sides are presented in Fig. 19a, b, respectively. Also, the mean hardness values for different regions (BM, HAZ, TMAZ, and SZ) across these dissimilar FSWs are reported and compared in Table 4. For the AA5052 alloy side (Fig. 19b), after employing of the FSW process, the hardness of the SZ and TMAZ regions was improved continuously due to grain structural refinements without any hardness loss in the HAZ. The maximum obtained hardness value was ~ 65.1 Vickers for processing parameters of $w = 1250$ rpm and $v = 160$ mm/min, in comparison to the

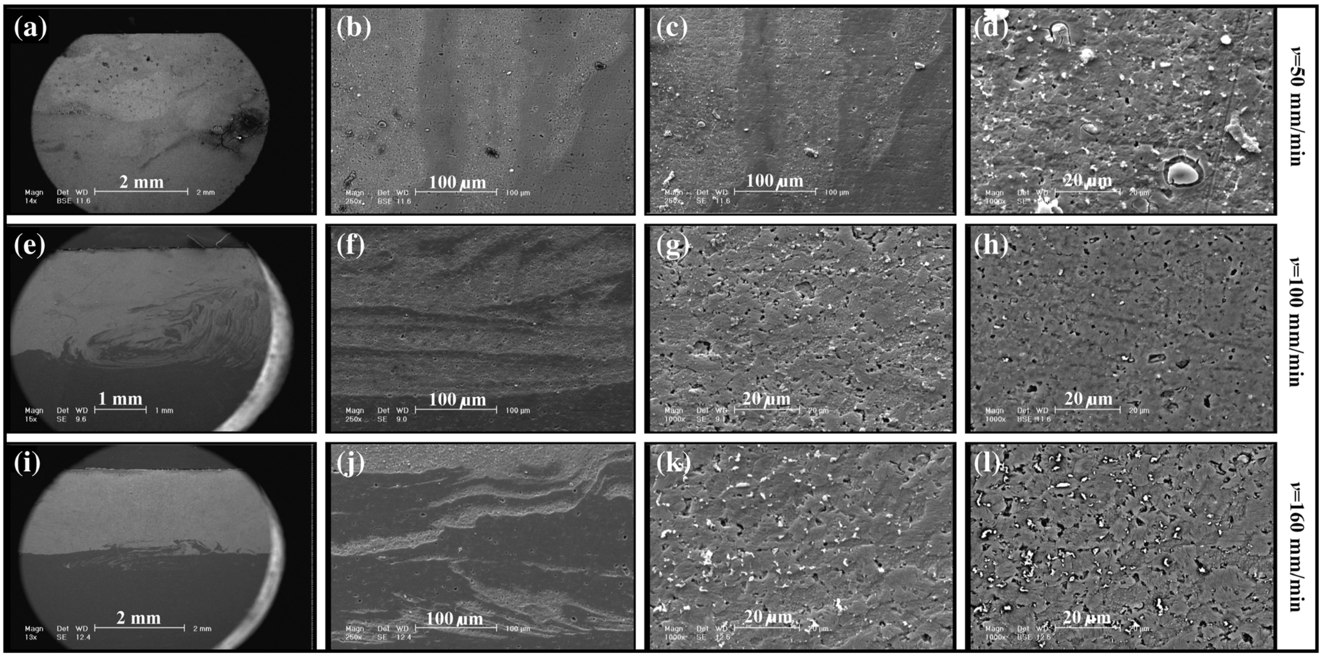

Fig. 17 Effects of traverse velocity on the SZ flow pattern, microstructure, and precipitates morphology for the dissimilar FSWed joints at rotational speed of 1250 rpm. **a**–**d** $v = 50$ mm/min, **e**–**h** $v = 100$ mm/min, and **i**–**l** $v = 160$ mm/min

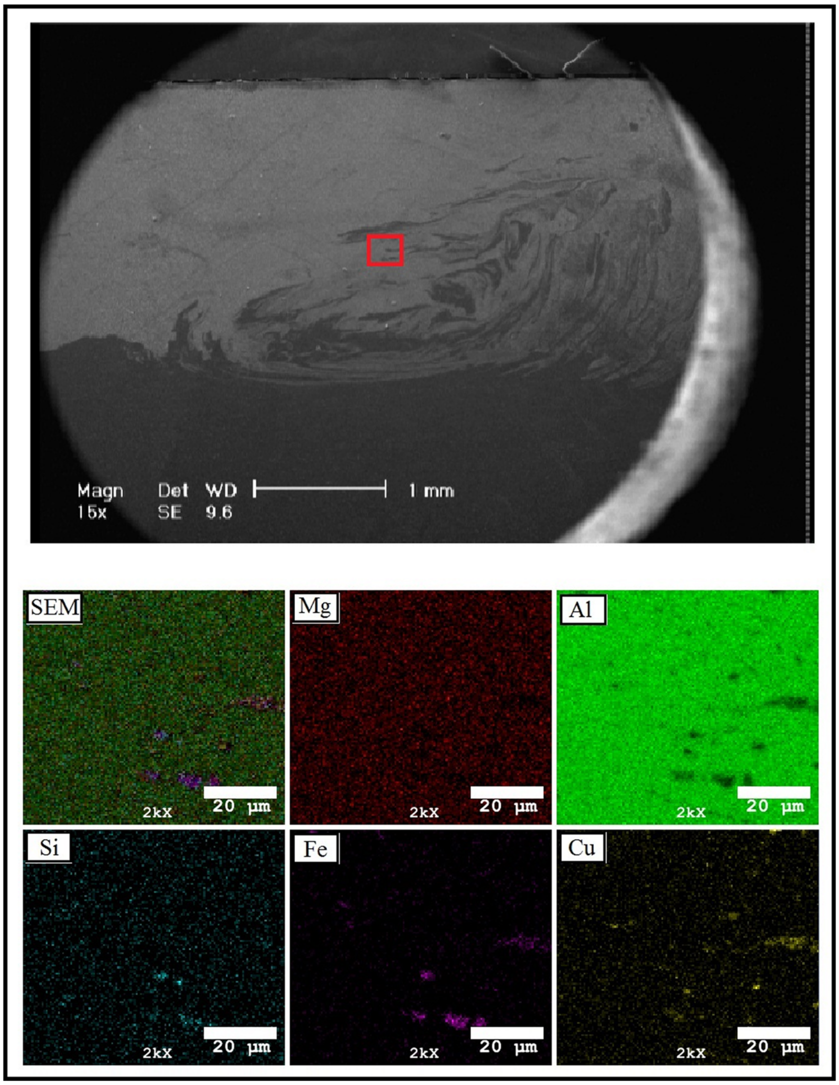

Fig. 18 FE-SEM image combined with the elemental EDS chemical analysis results from a selected region for the dissimilar FSWed joint at processing parameters of $w = 1250$ rpm and $v = 100$ mm/min

hardness of BM which was ~ 51.5 Vickers. These microhardness evolutions across the FSWed joint of the AA5052 alloy were reasonable considering this issue that it was utilized in the annealed or O temper condition. While, the microhardness trend was completely different at the AA2024 side (see Fig. 19a). Since, this alloy was used in the T4 temper condition and its microstructural histories disappeared completely during the FSW process and as a result a new microstructure containing new structure of precipitates with new sizes and new morphologies was produced. As seen, at HAZ and TMAZ regions, a significant hardness loss was occurred for this alloy, mainly due to precipitate coarsening and diminishing of previous cold work history [17]. This is a common phenomenon during FSW of precipitation harden-able aluminum alloys in the aged temper condition and reported variously for different alloys in the literature, as well [3]. For SZ, owing to the solution of precipitates during the FSW process and deterioration of previous cold work history, hardness can be decreased; however, the formation of a new structure from precipitates within the SZ and grain structural refinements during process can compensate these effects some deal [21]. As shown in Fig. 19b, at the best optimized processing condition, the hardness of SZ was kept at about 127.7 Vickers, which still was much lower than the AA2024-T4 base alloy with a hardness of about 138.1 Vickers. The main finding from these microhardness measurements was the mentioned extreme hardness gradients due to the microstructural modifications which can affect the mechanical performance of dissimilar FSWed joints during transverse tensile testing as follows.

3.6 Tensile flow behavior

Force-extension tensile flow curves of dissimilar FSWed joints at different processing parameters during transverse tensile testing up to the fracture point are presented and compared in Fig. 20a. Also, the main tensile properties versus the tool rotational speed and traverse velocity are plotted and reported in Fig. 20b and Table 5, respectively. As it can be obviously found, the best tensile properties including the highest tensile

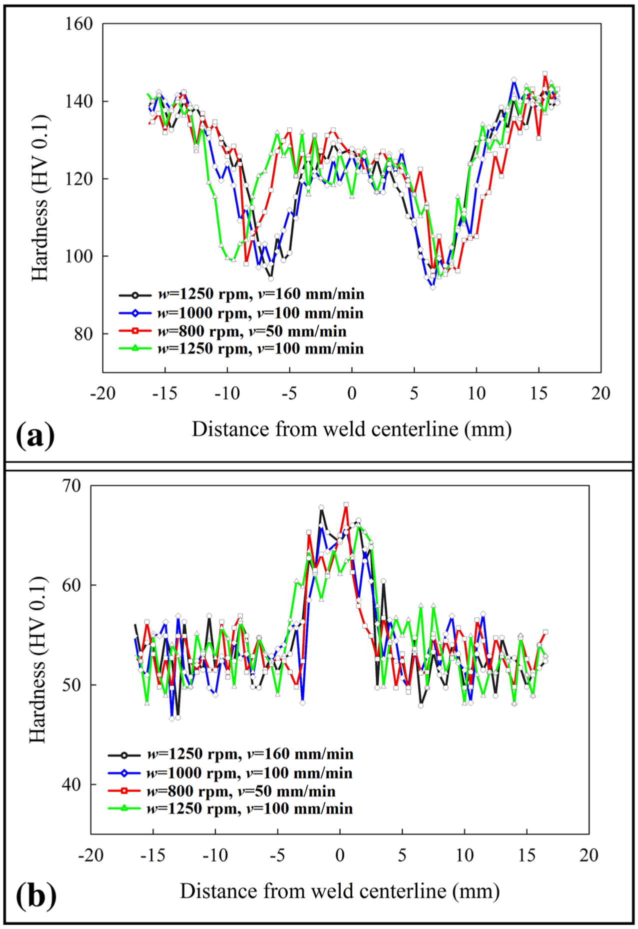

Fig. 19 Effects of the *w*/*v* ratio on the indentations Vickers microhardness profiles across the thickness sections at **a** AA2024 and **b** AA5052 regions of the processed dissimilar SZs. These measurements were only performed for the defect-free dissimilar joints

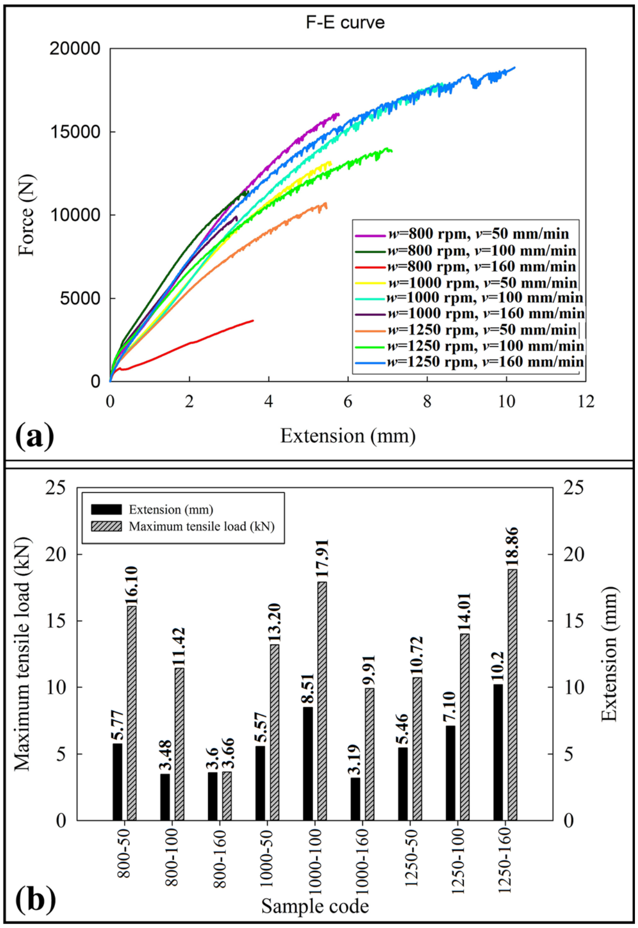

Fig. 20 **a** Load-extension tensile curves of the dissimilar FSWed joints at various rotational speeds and traverse velocities. **b** The main tensile properties versus processing parameters

fracture load (~ 19 kN) and highest elongation to failure (~ 10.2 mm) were owned to the processing parameter with higher *w* and *v* values, i.e., *w* = 1250 rpm and *v* = 160 mm/min. As described before in the macro- and microstructural sections, the processed dissimilar FSWed joint at this condition was completely sound and defect-free. Therefore, the highest tensile property for this sample was expectable. To find the reasons for the mentioned considerable differences between the tensile properties of this optimized sample with the other joints processed at different processing conditions, it is necessary to study the fracture behavior of these dissimilar joints during transverse tensile testing.

3.7 Fracture behavior and fractographic studies

Fracture locations for the transverse tensile tested dissimilar FSWed joints at different processing parameters are reported in Table 5. As seen, except for two samples, all of the other ones were failed from SZ. The processed dissimilar joint at FSW parameters of *w* = 1000 rpm and *v* = 100 mm/min were fractured from the HAZ of the AA2024 side. Also, dissimilar weld which showed the best tensile properties in processing conditions of *w* = 1250 rpm and *v* = 160 mm/min was failed from the AA5052 base alloy. It is due to the higher strength of SZ than AA5052 BM. FE-SEM images from the fracture surfaces of the dissimilar FSWed joints at different *w* and *v* parameters are demonstrated in Fig. 21. As can be found, the fractographic features on the fracture surface was completely related to the failure location across the dissimilar FSWs. For the failed sample from HAZ of the AA2024 side, a fine dimple-like structure in relation to the HAZ microstructure can be observed. However, for the failed dissimilar FSWed joints from SZ, the features on the fracture surfaces were completely different depending on the processing parameters and the related induced structural defects as preferred sites for crack nucleation. As an instance, for the FSW parameters of *w* = 800 rpm and *v* = 160 mm/min, the loose fracture surface show improper materials flow during dissimilar welding and weak metallurgical bonding. Considering the large ductility of Al-base alloy, this dissimilar weld sample did not showed considerable plastic deformation during fracture which

Table 4 The mean Vickers hardness values for different regions (BM, HAZ, TMAZ, and SZ) of the dissimilar FSWed joints at different w/v ratios from the AA2024 and AA5052 parts

Processing conditions		BM		HAZ		TMAZ		SZ	
Parameters	w/v ratio	AA2024 side	AA5052 side	AA2024 side	AA5052 side	AA2024 side	AA5052 side	AA2024 side	AA5052 side
w = 1250 rpm-v = 160 mm/min	7.8	138.1 ± 3.2	51.5 ± 1.6	117.6 ± 20.5	51.5 ± 1.6	109.8 ± 12.7	54.2 ± 2.9	122.5 ± 4.2	65.1 ± 2.9
w = 1000 rpm-v = 100 mm/min	10	138.1 ± 3.2	51.5 ± 1.6	117.5 ± 20.6	51.5 ± 1.6	108.7 ± 11.6	55.5 ± 3.4	120.3 ± 5.1	62.5 ± 4.2
w = 1250 rpm-v = 100 mm/min	12.5	138.1 ± 3.2	51.5 ± 1.6	118.5 ± 19.5	51.5 ± 1.6	112.3 ± 13.3	53.1 ± 2.2	125.6 ± 6.4	62.0 ± 3.8
w = 800 rpm-v = 50 mm/min	16	138.1 ± 3.2	51.5 ± 1.6	118.1 ± 20.0	51.5 ± 1.6	112.9 ± 14.9	56.9 ± 5.2	127.7 ± 3.3	64.6 ± 3.3

Table 5 Effects of processing parameters on the main tensile properties and fracture location of the dissimilar FSWed joints during transverse tensile testing

Traverse velocity (mm/min)	Rotational speed (w)								
	w = 800 rpm	w = 1000 rpm	w = 1250 rpm	w = 800 rpm	w = 1000 rpm	w = 1250 rpm	w = 800 rpm	w = 1000 rpm	w = 1250 rpm
	Maximum tensile load (kN)			Extension (mm)			Fracture location		
v = 50 mm/min	16.10	13.20	10.72	5.77	5.57	5.46	SZ	SZ	SZ
v = 100 mm/min	11.42	17.91	14.01	3.48	8.51	7.10	SZ	HAZ/AA2024	SZ
v = 160 mm/min	3.66	9.91	18.86	3.6	3.19	10.2	SZ	SZ	BM/AA5052

Fig. 21 FE-SEM images demonstrating the influence of *w*/*v* ratio on the fracture surface of dissimilar FSWed joints between AA5052 and AA2024 alloys: **a** w=800 rpm/v=160 mm/min, **b** w=1000 rpm/v=160 mm/min, **c** w=1250 rpm/v=160 mm/min, **d** w=800 rpm/v=100 mm/min, **e** w=1000 rpm/v=100 mm/min, **f** w=1250 rpm/v=100 mm/min, **g** w=800 rpm/v=50 mm/min, **h** w=1000 rpm/v=50 mm/min, and **i** w=1250 rpm/v=50 mm/min

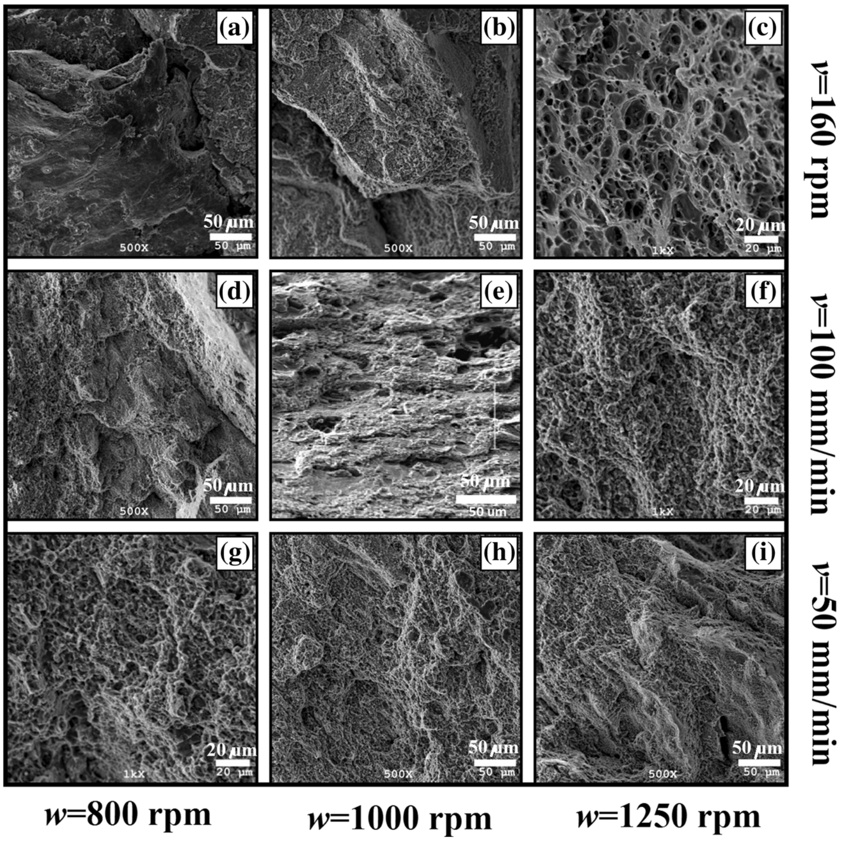

indicates the poor materials inter-mixing. As another example, on the fracture surface of processed dissimilar joint with the highest heat input, i.e., *w* = 1250 rpm and *v* = 50 mm/min, formation of some voids was observed, probably due to the turbulent flow of plasticized material during the FSW process. In a simple comparison between Fig. 21g–i, it can be found that with decreasing the rotational speed at a constant traverse velocity of 50 mm/min, the size of dimples becomes larger in correlation to their toughness as displayed in Fig. 20a. The same trend can be considered with increasing *v* at a constant *w* = 1250 rpm (see Fig. 21c–i). On the fracture surface of only sample failed from the AA5052 base alloy, large and deep dimples were observed because of failure occurrence from a BM with superior ductility.

4 Discussion

During dynamic restoration phenomena, the material flow behavior, microstructural features, and mechanical properties are mainly controlled by the Zener-Hollomon parameter as below [27]:

$$Z = \dot{\varepsilon}\exp\left({}^{Q}/_{RT}\right) \tag{1}$$

where $\dot{\varepsilon}$ is the strain rate, Q is the activation energy, R is the universal gas constant, and T is the working temperature. The mean grain size versus the Zener-Holloman parameter is plotted in Fig. 22. A linear relationship with a minus slope as follows is seen:

$$\ln(Z) = -4.0\ln(d) - 30.7 \tag{2}$$

Therefore, it can be expressed that increscent of the Z parameter by raising the flow stress and generation of dislocations posses an impact influence on the grain structural refinements. In the literature [28], several dynamic restoration mechanisms have been discussed as operative for microstructural

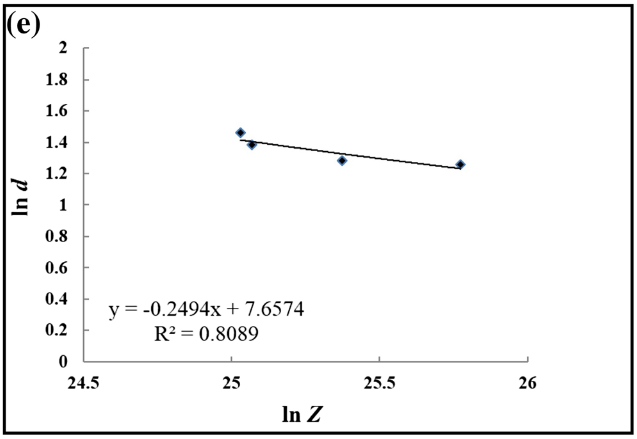

Fig. 22 Zener-Hollomon equation for these processed dissimilar welds

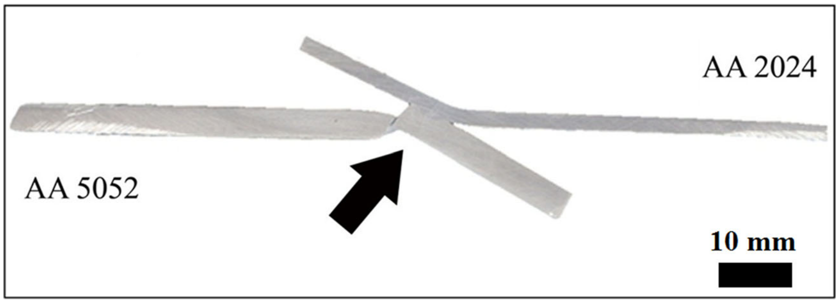

Fig. 23 A macro-image from the failure behavior of the dissimilar FSWed AA5052-AA2024 joint processed at *w* = 1250 rpm and *v* = 160 mm/min during transverse tensile loading

refinements during FSW/FSP processes depending on the examined metals/alloys and processing conditions, including dynamic recovery (DRV), continuous dynamic recrystallization (CDRX), discontinuous dynamic recrystallization (DDRX), and geometric dynamic recrystallization (GDRX). However, there is a large debate among the researchers about the dominant restoration mechanisms during friction-stir welding/processing of different aluminum alloys by considering their stacking fault energy. Materials mixing, mechanical interlocking, grain structural refinement according to the Hall-Petch relation, formation and distribution of different secondary phase precipitates according to the Orowan looping mechanism, and formation of Al-Mg-Si-Cu intermetallic phases can be considered as the main strengthening mechanisms for the SZ of prepared AA5052-AA2024 dissimilar joints during FSW bonding [24]. As the main finding of the present research, processing parameters of *w* = 1250 rpm and *v* = 160 mm/min with the *w*/*v* ratio of 7.8 rpm.min/mm are introduced as the optimum conditions for dissimilar friction-stir lap-welding of AA5052-O and AA2024-T4 aluminum alloys with an exceptional mechanical performance.

A macro-image from the transverse tensile failure behavior of this dissimilar FSWed joint is presented in Fig. 23. The effective thickness of the lap joint design which exerts a significant effect on the mechanical properties is mainly controlled by the hook and cold lap defects [3]. During dissimilar lap-welding, the faying surface at the advancing side remains outside the SZ and folds upward along the nugget boundary which is known as the hook defect [29]. However, cold lap defect is due to the lifting up and penetration of faying surface into the weld nugget [30]. These hook and cold lap defects are mainly the reflections of material flow patterns at the faying surface of the lap joint, and subsequently, these profiles were affected by the geometrical specifications of the FSW tool and processing parameters [30]. Therefore, optimization of processing parameters can contribute to minimization of such defects which enhance the mechanical performance of lap joint designs and their fracture behavior, as well. The correlation between microstructure, joint performance, and fracture behavior can be explained based on formation of hook defect at the advancing side [16]. The results showed that the effective thickness of the top AA2024 sheet was reduced as caused by the influence of hook defect. Meanwhile, the level of this sheet thinning was gradually decreased by decreasing of tool rotational speed and increasing of traverse velocity.

5 Conclusions

The feasibility of dissimilar solid-state joining between an Al-Mg alloy (AA5052) and an Al-Cu alloy (AA2024) by the friction-stir welding process in lap joint design was assessed. The effects of processing parameters and joint design on the microstructure and mechanical properties of dissimilar FSWs were addressed. The main findings can be expressed as follows:

- With increasing *w* and decreasing *v* (or increasing the *w*/*v* ratio), the peak temperature at all locations of the advancing side, retreating side, and center line was increased, continuously with a maximum value of about 550 °C.
- The material inter-mixing patterns between these dissimilar alloys were completely changed by variations of thermal history depending on the heat input parameter in terms of the *w*/*v* ratio during the FSW process.
- A mechanical softening was occurred in the HAZ and TMAZ regions at the AA2024 side due to grain growth and coarsening of copper aluminide precipitates.
- Completely different fractographic features were determined depending on the failure location as varied by the processing conditions.
- The joint design which includes locating the AA2024 alloy at the top side with employing the processing parameters of *w* = 1250 rpm and *v* = 160 mm/min leads to fabrication of a dissimilar joint with the best dissimilar materials inter-mixing and subsequently proper mechanical properties. Fracture of this welding sample was occurred from the AA5052 side, as the weakest BM. A completely ductile fracture surface with large dimples was noticed for this sample.
- The microstructure-mechanical properties relationship was elaborated for the optimized dissimilar FSW, with describing the grain structural refinement based on the Zener-Hollomon parameter (Z) as the main strengthening mechanism.

References

1. Cole GS, Sherman AM (1995) Light weight materials for automotive applications. Mater Charact 35:3–9
2. Benedyk JC. 3 - Aluminum alloys for lightweight automotive structures A2 - Mallick, P.K. Materials, design and manufacturing for lightweight vehicles. Woodhead Publishing, 2010. p.79–113
3. da Silva AAM, Arruti E, Janeiro G, Aldanondo E, Alvarez P, Echeverria A (2011) Material flow and mechanical behaviour of dissimilar AA2024-T3 and AA7075-T6 aluminium alloys friction stir welds. Mater Des 32:2021–2027
4. Khodabakhshi F, Gerlich AP, Simchi A, Kokabi AH (2015) Cryogenic friction-stir processing of ultrafine-grained Al–Mg–TiO_2 nanocomposites. Mater Sci Eng A 620:471–482
5. Yan Y, Zhang DT, Qiu C, Zhang W (2010) Dissimilar friction stir welding between 5052 aluminum alloy and AZ31 magnesium alloy. Trans Nonferrous Metals Soc China 20:619–623
6. Schmidt HNB, Dickerson TL, Hattel JH (2006) Material flow in butt friction stir welds in AA2024-T3. Acta Mater 54:1199–1209
7. Ma H, Qin G, Bai X, Wang L, Liang Z (2016) Effect of initial temperature on joint of aluminum alloy to galvanized steel welded by MIG arc brazing-fusion welding process. Int J Adv Manuf Technol 86:3135–3143
8. Wei HL, Elmer JW, DebRoy T (2016) Origin of grain orientation during solidification of an aluminum alloy. Acta Mater 115:123–131
9. Olea CAW, Roldo L, Strohaecker TR, Dos Santos JF (2006) Friction stir welding of precipitate hardenable aluminium alloys: a review. Welding in the World 50:78–87
10. Mishra RS, Ma ZY (2005) Friction stir welding and processing. Materials Science and Engineering: R: Reports 50:1–78
11. Neto DM, Neto P (2013) Numerical modeling of friction stir welding process: a literature review. Int J Adv Manuf Technol 65:115–126
12. Khodabakhshi F, Haghshenas M, Sahraeinejad S, Chen J, Shalchi B, Li J, Gerlich AP (2014) Microstructure-property characterization of a friction-stir welded joint between AA5059 aluminum alloy and high density polyethylene. Mater Charact 98:73–82
13. Hattel JH, Sonne MR, Tutum CC (2014) Modelling residual stresses in friction stir welding of Al alloys—a review of possibilities and future trends. Int J Adv Manuf Technol 76:1793–1805
14. Ghosh M, Kumar K, Kailas SV, Ray AK (2010) Optimization of friction stir welding parameters for dissimilar aluminum alloys. Mater Des 31:3033–3037
15. Nandan R, DebRoy T, Bhadeshia HKDH (2008) Recent advances in friction-stir welding—process, weldment structure and properties. Prog Mater Sci 53:980–1023
16. Palanivel R, Koshy Mathews P, Murugan N, Dinaharan I (2012) Effect of tool rotational speed and pin profile on microstructure and tensile strength of dissimilar friction stir welded AA5083-H111 and AA6351-T6 aluminum alloys. Mater Des 40:7–16
17. Cavaliere P, Panella F (2008) Effect of tool position on the fatigue properties of dissimilar 2024-7075 sheets joined by friction stir welding. J Mater Process Technol 206:249–255
18. Jonckheere C, de Meester B, Denquin A, Simar A (2013) Torque, temperature and hardening precipitation evolution in dissimilar friction stir welds between 6061-T6 and 2014-T6 aluminum alloys. J Mater Process Technol 213:826–837
19. Rodriguez RI, Jordon JB, Allison PG, Rushing T, Garcia L (2015) Microstructure and mechanical properties of dissimilar friction stir welding of 6061-to-7050 aluminum alloys. Mater Des 83:60–65
20. Bozkurt Y, Bilici MK (2013) Application of Taguchi approach to optimize of FSSW parameters on joint properties of dissimilar AA2024-T3 and AA5754-H22 aluminum alloys. Mater Des 51: 513–521
21. Koilraj M, Sundareswaran V, Vijayan S, Koteswara Rao SR (2012) Friction stir welding of dissimilar aluminum alloys AA2219 to AA5083—optimization of process parameters using Taguchi technique. Mater Des 42:1–7
22. Tang J, Shen Y (2016) Numerical simulation and experimental investigation of friction stir lap welding between aluminum alloys AA2024 and AA7075. J Alloys Compd 666:493–500
23. Costa MI, Verdera D, Leitão C, Rodrigues DM (2015) Dissimilar friction stir lap welding of AA 5754-H22/AA 6082-T6 aluminium alloys: influence of material properties and tool geometry on weld strength. Mater Des 87:721–731
24. Khodabakhshi F, Simchi A, Kokabi AH, Gerlich AP (2016) Similar and dissimilar friction-stir welding of an PM aluminum-matrix hybrid nanocomposite and commercial pure aluminum: microstructure and mechanical properties. Mater Sci Eng A 666:225–237
25. Khodabakhshi F, Simchi A, Kokabi AH, Gerlich AP, Nosko M (2015) Effects of stored strain energy on restoration mechanisms and texture components in an aluminum–magnesium alloy prepared by friction stir processing. Mater Sci Eng A 642:204–214
26. Song Y, Yang X, Cui L, Hou X, Shen Z, Xu Y (2014) Defect features and mechanical properties of friction stir lap welded dissimilar AA2024–AA7075 aluminum alloy sheets. Mater Des 55:9–18
27. McNelley TR, Swaminathan S, Su JQ (2008) Recrystallization mechanisms during friction stir welding/processing of aluminum alloys. Scr Mater 58:349–354
28. Murr LE, Pizaña C (2007) Dynamic recrystallization: the dynamic deformation regime. Metallurgical and Materials Transactions A: Physical Metallurgy and Materials Science 38(A):2611–2628
29. Khan NZ, Siddiquee AN, Khan ZA, Shihab SK (2015) Investigations on tunneling and kissing bond defects in FSW joints for dissimilar aluminum alloys. J Alloys Compd 648:360–367
30. Xu Z, Li Z, Lv Z, Zhang L (2017) Effect of tool rotating speed on microstructure and mechanical properties of friction stir lap welded Ti–6Al–4V alloy. Int J Adv Manuf Technol 90:3793–3800